Sensors & Actuators: B. Chemical 329 (2021) 129145

Contents lists available at ScienceDirect

Sensors and Actuators: B. Chemical

journal homepage: www.elsevier.com/locate/snb

The influence of different ZnO nanostructures on NO_2 sensing performance

Hongtao Wang, Meng Dai, Yueyue Li, Jihao Bai, Yueying Liu, Yuan Li, Chenchang Wang, Fengmin Liu *, Geyu Lu *

State Key Laboratory on Integrated Optoelectronics, College of Electronic Science and Engineering, Jilin University, 2699 Qianjin Street, Changchun 130012, China

ARTICLE INFO

Keywords:
NO_2 sensor
Morphology-dependent
ZnO
UV
Room temperature

ABSTRACT

Three different ZnO nanostructures (nanorods/flowers/spheres) were prepared through facile hydrothermal method or water bath, whose sensing properties to NO_2 were investigated in detail at room temperature activated by UV light (365 nm LED). The sensing results showed that ZnO nanospheres exhibit the highest response of 29.4–5 ppm NO_2, which can be attributed to their biggest specific surface area and the most amount of adsorbed oxygen species on the surface. In contrast, ZnO nanorods show the fastest response and recovery speed (9 and 18 s to 5 ppm NO_2, respectively) due to their highest crystallinity, least surface defects and unidirectional electron transfer path, which is much faster than most reported literatures. With regard to the ZnO nanoflowers, both the gas-sensing response and the response and recovery speed are between ZnO nanorods and ZnO nanospheres. Furthermore, the stability, selectivity, and the moisture resistance of three different ZnO nanostructures were also researched.

1. Introduction

With the improvement of living standard, air pollution has attracted more and more attention and research. As one of the nitrogen oxides, NO_2 mainly comes from fossil fuels, automobile exhaust, and factory fumes and seriously endangers the environment and human health [1,2]. More seriously, long-term exposure to high concentrations of NO_2 can significantly increase the incidence of acute respiratory disease in children [3,4]. Therefore, the accurate detection of NO_2 gas in the atmosphere has great significance to environmental protection and human health.

In recent years, NO_2 gas sensors based on MOS has been widely researched because of their low-cost synthesis, high sensitivity, fast response and recovery speed, and good stability [5,6]. However, the sensors usually need to be heated to a few hundred degrees to facilitate the adsorption of harmful gases and subsequent gas-sensing reactions, which not only causes energy consumption but also affects the stability and safety of the sensors, especially when flammable and explosive gases are present [7,8]. Therefore, NO_2 sensors based on MOS need further research and improvement.

UV irradiation instead of heating method is an effective approach to reduce the initial resistance and activate the surface of sensing nanomaterials [9,10]. The photosorbed negative oxygen species generated by capturing photogenerated electrons is more reactive than the chemisorbed negative oxygen species, and the photogenerated holes also can promote the desorption of NO_2 [11,12]. Furthermore, UV light excitation has less influence on the nanostructure of sensing materials than the traditional heating method, which is also more suitable for integrated wearable gas sensors [13].

ZnO, as a typical direct band gap semiconductor, was widely applied in NO_2 gas sensors activated by UV light due to its excellent light absorption and appropriate band gap (3.2 eV) [14]. For example, Qi et al. have successfully prepared ZnO nanowalls in situ on porous rGO to detect NO_2 under UV irradiation at room temperature [15]. Meng et al. activated ZnO microwire with a combined technology of surface etching and UV illumination to realize the detection of NO_2 gas [16]. However, poor sensitivity and lengthy response and recovery speed seriously restrict the development of NO_2 sensors based on ZnO activated by UV light. Therefore, researchers still need to develop more promising ZnO nanomaterials for NO_2 sensors activated by UV light.

Here, three different ZnO nanostructures (nanorods/flowers/spheres) were successfully prepared by facile hydrothermal method or water bath. The nanostructure-dependent NO_2 sensing performance activated by UV light (365 nm LED) was investigated in detail at room temperature. The sensing results showed that as-prepared three different ZnO nanostructures exhibit huge differences in sensitivity and the response and recovery speed. We attempted to explain this phenomenon from multiple perspectives with the help of a variety of characterization

* Corresponding authors.
E-mail addresses: liufm@jlu.edu.cn (F. Liu), lugy@jlu.edu.cn (G. Lu).

https://doi.org/10.1016/j.snb.2020.129145
Received 31 March 2020; Received in revised form 24 October 2020; Accepted 2 November 2020
Available online 7 November 2020

methods and describe the detailed gas-sensing process under UV light in this work.

2. Experimental section

2.1. Materials

All reagents – Zinc nitrate hexahydrate ($Zn(NO_3)_2{\cdot}6H_2O$), sodium hydroxide (NaOH), cetyltrimethylammonium bromide (CTAB), methenamine ($C_6H_{12}N_4$), trisodium citrate dihydrate ($C_6H_5Na_3O_7{\cdot}2H_2O$) were purchased from Aladdin Reagent Co., Ltd. (Shanghai, China), and were of analytic grade and used as received without further purification. Deionized water was used as a solvent to prepare solution.

2.2. Preparation of three different ZnO nanostructures

The ZnO nanorods were synthesized through facile hydrothermal method. 7.8 mmol of $Zn(NO_3)_2{\cdot}6H_2O$ was dissolved into 20 ml of distilled water under vigorous stirring. 48 mmol of NaOH and 0.2 mmol of CTAB were dissolved into 20 ml of distilled water to form a transparent solution under continuous stirring. Then, mixing the two above solution and remaining stirring for 30 min. The resulted solution was transferred to a Teflon-lined stainless steel autoclave with a capacity of 50 ml, and heated at 90 °C for 15 h. The precipitate on the bottom was centrifuged with distilled water and ethanol for three times and dried in an oven at 60 °C for 6 h. Finally, the white powder was calcined at 400 °C for 2 h with a heating rate of 10 °C/min in a muffle furnace.

The ZnO nanoflowers were synthesized as follows. 0.891 g of $Zn(NO_3)_2{\cdot}6H_2O$ was dissolved into 30 ml of distilled water under vigorous stirring. 0.72 g of NaOH was dissolved into above solution and adding 0.109 g of CTAB. After stirring for 1 h, the resulted solution was transferred to a Teflon-lined stainless steel autoclave with a capacity of 100 ml, and heated at 150 °C for 16 h. The process of subsequent centrifugal purification and calcination was as same as the ZnO nanorods.

The ZnO nanospheres were prepared by water bath. In a typical procedure, 3 mmol of $Zn(NO_3)_2{\cdot}6H_2O$ was added to a beaker containing 100 mL of deionized water under vigorous stirring. 9 mmol of $C_6H_{12}N_4$ and 0.8 mmol of $C_6H_5Na_3O_7{\cdot}2H_2O$ were dissolved in another beaker containing 100 mL of deionized water under vigorous stirring. Keep stirring for 20 min to obtain two clarified precursor solutions. Then the above two precursor solutions were transferred into a three-necked bottle with a capacity of 250 ml, and heated at 90 °C for 2 h under stirring in a water bath kettle with reflux unit. The process of subsequent centrifugal purification and calcination was also as same as the ZnO nanorods.

2.3. Characterization

X-ray diffraction (XRD) measurements were conducted to explore the crystallinity and phase composition of as-prepared ZnO on a Rigaku D/MAX-2550 diffractometer using Cu-Kα radiation (λ =0.15418 nm). The morphology characteristics were investigated by field-emission scanning electronic microscope (FESEM, Carl Zeiss Sigma 500 V P) and transmission electron microscope (TEM, JEM-2100 F, JEOL). UV–vis (UV–vis) absorption spectra were measured by a UV–vis spectrophotometer (Shimadzu UV2550, Japan). The information related to the element composition and surface oxygen states in three different ZnO nanostructures were collected by using VG Multilab 2000 (Thermo Scientific) X-ray photoelectron spectroscopy (XPS). N_2 adsorption-desorption analysis (Autosorb-iQ2ST/MP Quantachrome) was carried out to measure the Brunauer-Emmett-Teller (BET) surface area of three different ZnO nanostructures. Impedance spectroscopy was measured on an electrochemical workstation (CHI660D, Shanghai Chenhua Instrument Co., Ltd, China). The initial electric potential is 0.2454 V, the frequency range for impedance measurement is 0.01 to 1e+6 Hz, and the amplitude is 0.005 V.

2.4. Fabrication and measurement of gas sensors

The fabrication process of sensors has been described in detail in our previously reported literatures [17,18]. A certain quantity of as-prepared ZnO was dispersed into a trace of ethanol and formed a slurry. The slurry was coated on the outside surface of a ceramic tube using a brush, whose four corners have platinum wires for transmitting signals. Then the ceramic tube was calcined at 300 °C for 2 h in a muffle furnace to solidify the sensing layer. Finally, the ceramic tube was welded to a six-legged base. The as-fabricated sensor element needs to be aged for three days before conducting gas sensitivity tests to obtain a stable baseline. If we test the sensor devices directly without aging, the baseline resistance is difficult to stabilize. A UV-LED (λ = 365 nm, LG Electronics Co. Ltd., South Korea) was installed on the top of the sensor element to motivate the sensor. The applied voltage of the UV-LED light source is 3.5 V, and the power is 3 W. The graphical model of the sensor element was shown in Fig S1a and b. It is worth mentioning that the Ni-Cr alloy only used for aging the sensor element.

The gas sensitivity test system in this work is static. When the resistance of sensor element was stable in a gas chamber containing pure air, the sensor element was moved to another gas chamber containing a certain concentration of NO_2. After its resistance was stabilized in NO_2 atmosphere, the sensor element was removed to the pure air again. The exposure time of all the sensor devices in NO_2 was 150 s, and the subsequent exposure interval in air was 250 s. It is important to note that there is no change in atmosphere of the gas chambers during the movement. If both gas chambers contain pure air, the transfer process will cause a slight fluctuation in resistance and then quickly return back to the baseline, not have a big change. The tiny change in resistance during the transferring between two gas chambers are due to the indoor airflow. The sensor device was briefly exposed to indoor airflow during the transfer, which has different effects on the resistance. Therefore, the resistance would have a slight fluctuation (about 5%) and then quickly return back to the baseline after transfer to the second chamber. This change in resistance is not due to the difference between the air in the two gas chambers, which is only temporary. In addition, the relative humidity was maintained at 30 % throughout the sensing measurements. A constant temperature humidity chamber (Shanghai Espek Environmental Equipment Co., LTD) was used to create different humidity atmosphere to explore the effect of humidity on the response. Different concentrations of NO_2 atmosphere were obtained by mixing pure air and 500 ppm standard NO_2 gas, which was purchased from Juyang Gas Co., Ltd. (Changchun, China). The resistance of sensor element was measured by a multimeter (Fluke 8846A) powered by a direct current and recorded in real time by a data-acquisition PC. The response was defined as $S = R_g/R_a$, where R_g and R_a are the resistance of sensor element after exposing to NO_2 gas and the initial resistance in pure air. The response and recovery time were defined as the time taken by the sensor element to achieve 90 % of the total resistance change. The diagram of gas sensitivity test system was shown in Fig. S1c.

3. Results and discussion

3.1. Characterization

Fig. 1 showed the XRD patterns of as-prepared ZnO. All samples show eleven main diffraction peaks, which match well with Bragg reflections of the standard hexagonal wurtzite ZnO structure (JCPDS card no. 36–1451) [19]. In addition to the peaks of ZnO, no other impurity diffraction peaks were detected. Furthermore, it can be seen that the intensity of ZnO nanorods are obviously stronger than those of ZnO nanoflowers and ZnO nanospheres, which indicates its highest crystallinity. Generally speaking, higher crystallinity results in less grain boundary, which benefits the electron transfer [20]. The crystal sizes of three different ZnO nanostructures were calculated using Scherrer's formula [21]:

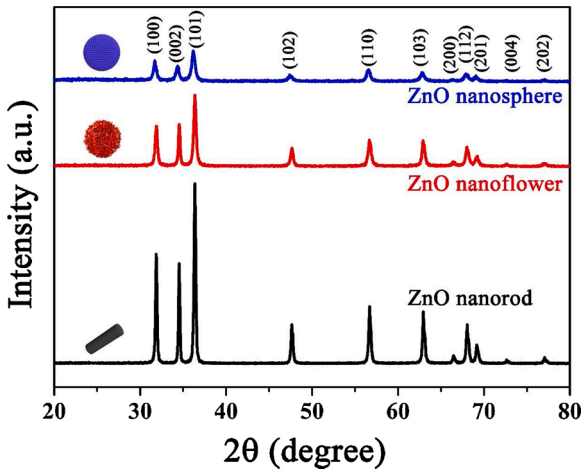

Fig. 1. XRD patterns of three different ZnO nanostructures.

$$D = \frac{K\lambda}{\beta cos\theta} \quad (1)$$

where k is the Scherrer constant, λ is the wavelength of X-ray of Cu kα-line, β is the calculated full width at half maxima (FWHM) and θ is the Bragg's angle. The calculated average crystal sizes of ZnO nanorods, ZnO nanoflowers, and ZnO nanospheres were 50.2, 31.7, and 19.6 nm, respectively.

The morphology characteristics of as-prepared ZnO were analyzed by FESEM and displayed in Fig. 2. As shown in Fig. 2a and b, ZnO nanorods exhibit irregular diameter and length. The diameter is roughly ranging from 50 to 300 nm and the length is about 1–2 μm. From the high-resolution FESEM image, it can be seen that ZnO nanorods have smooth surface and high crystallinity. Fig. 2c and d showed that ZnO nanoflowers are composed of uniform nanosheets with length of 200–300 nm and the thickness is about 30 nm. With regard to ZnO nanospheres, they exhibit porous and rough surface due to the gas bubbles of formaldehyde and ammonia produced by the decomposition of $C_6H_{12}N_4$ during the water bath. From Fig. 2e, it also can be seen that parts of ZnO nanospheres possess macropore structure, which is beneficial to increase the specific surface area and promote the adsorption of tested gases. The enlarged FESEM image in Fig. 2f showed that ZnO

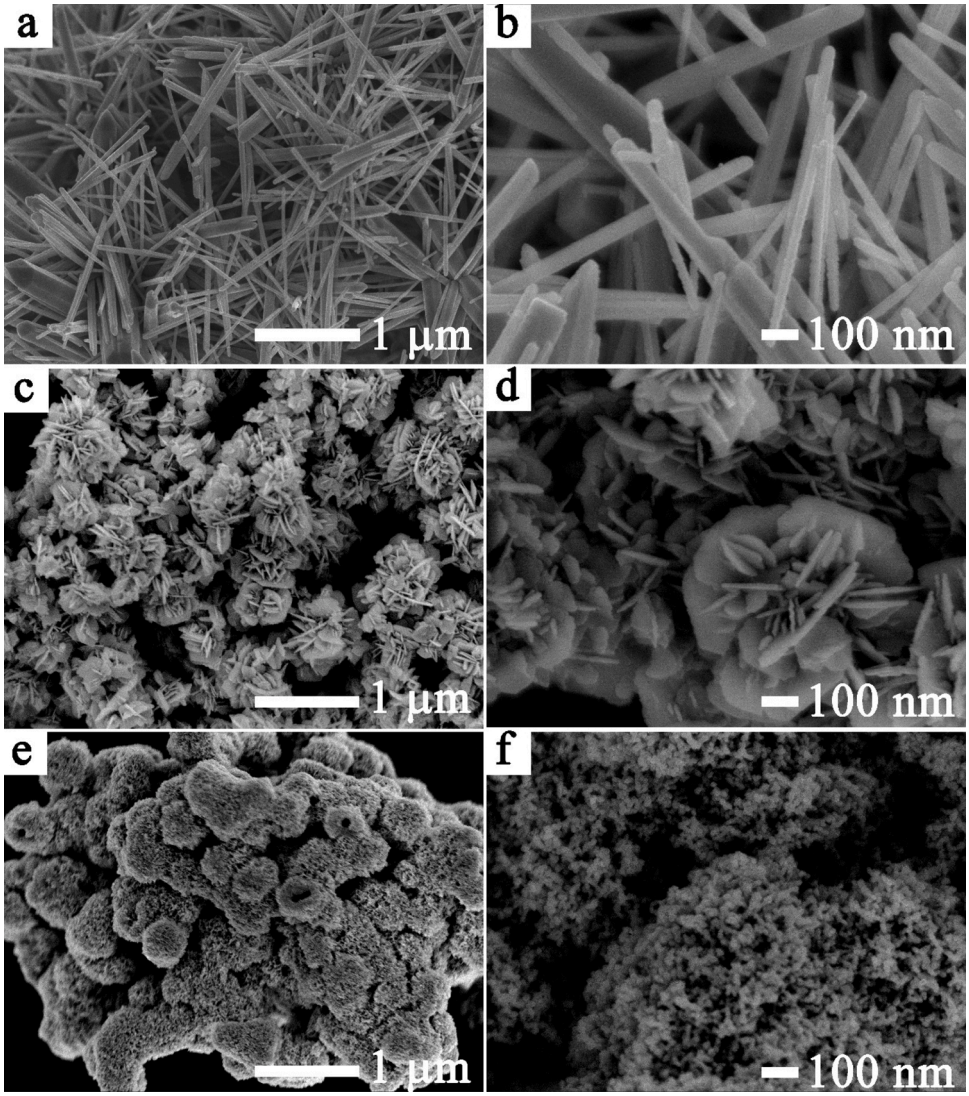

Fig. 2. Low- and high-resolution SEM images of (a–b) ZnO nanorods, (c–d) ZnO nanoflowers, (e–f) ZnO nanospheres.

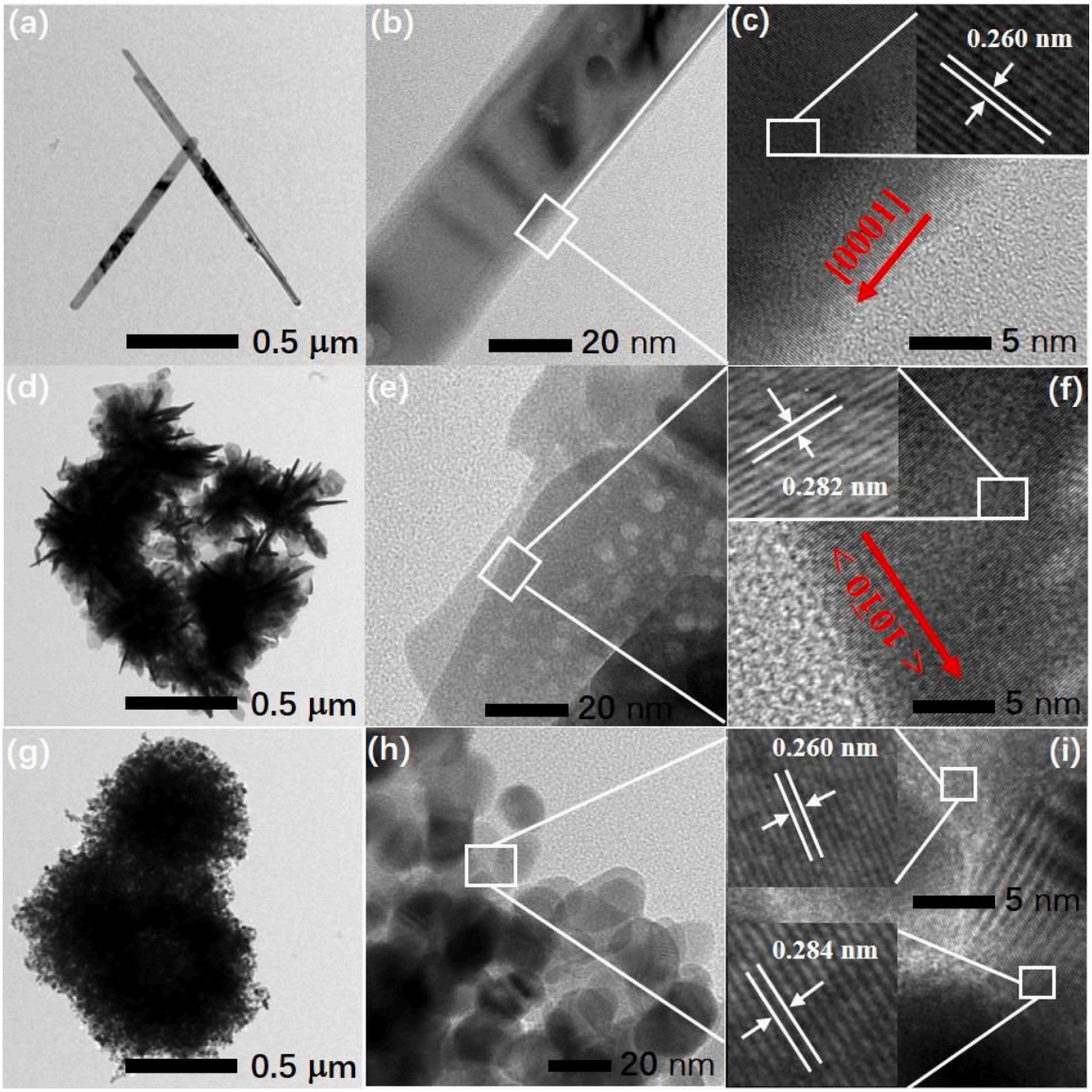

Fig. 3. TEM images and the corresponding lattice fringe of (a–c) ZnO nanorods, (d–f) ZnO nanoflowers, (g–i) ZnO nanospheres.

nanospheres consists of tiny nanoparticles, whose diameter is about 20–30 nm.

The TEM images of ZnO nanorods, nanoflowers, and nanospheres were shown in Fig. 3(a–c), Fig. 3(d–f), and Fig. 3(g–i), respectively. The sizes and morphologies of three different ZnO nanostructures in TEM images are both in accordance with the results of FESEM. From Fig. 3c, it can be seen that the lattice fringes of ZnO nanorods are very clear and regular, indicating its good crystallinity. The lattice fringe spacing of 0.260 nm matches well with (0002) plane of hexagonal wurtzite ZnO, which indicates that $\left\{10\bar{1}0\right\}$ facet of ZnO nanorods grows along the c axis [22]. In contrast, lattice disorder and deletion phenomenon can be observed in the HRTEM images of ZnO nanoflowers and nanospheres due to their more surface defects, which were shown in Fig. 3f and i. The lattice fringe spacing of ZnO nanoflowers is 0.282 nm, corresponding to the $\left(10\bar{1}0\right)$ plane of hexagonal wurtzite ZnO. It indicated that {0001} facet of ZnO nanoflowers grows along the direction of $< 10\bar{1}0 >$ [23]. With regard to ZnO nanospheres, two kinds of lattice fringe spacing about 0.284 nm $\left(10\bar{1}0\right)$ and 0.260 nm (0002) were both observed, which indicates that the growth direction is irregular.

Fig. 4a presented the UV–vis absorption spectra of three different ZnO nanostructures. All of the ZnO showed a strong absorption in the UV light region due to their wide bandgap. The relationship of bandgap and absorbance of ZnO can be described by the following Eq. [24].

$$\alpha h\nu = A(h\nu - E_g)^n \quad (2)$$

where α, hν, E_g and A represent the optical absorption coefficient, photon energy, band gap and proportionality constant, respectively. For the direct bandgap semiconductors, n is 1/2; for indirect semiconductors, n is 2. The estimated bandgap of ZnO nanorods, nanoflowers, and nanospheres is 3.08, 3.19, and 3.24 eV, respectively, as shown in Fig. 4b. It is generally accepted that the optical bandgap is closely related to the crystal defect concentration, which can induce a redshift of absorption edge [25]. Therefore, it can be inferred that ZnO nanorods have the least defect concentration while ZnO nanospheres have the most.

XPS were conducted to investigate the surface elemental composition and oxygen states. As shown in Fig. 5, two peaks of Zn 2p located at 1021.1 and 1044.2 eV, which can be corresponded to the Zn $2p_{3/2}$ and Zn $2p_{1/2}$, respectively [26]. The O 1s spectra were deconvoluted into two peaks at 529.4 and 530.9 eV, corresponding to the lattice oxygen

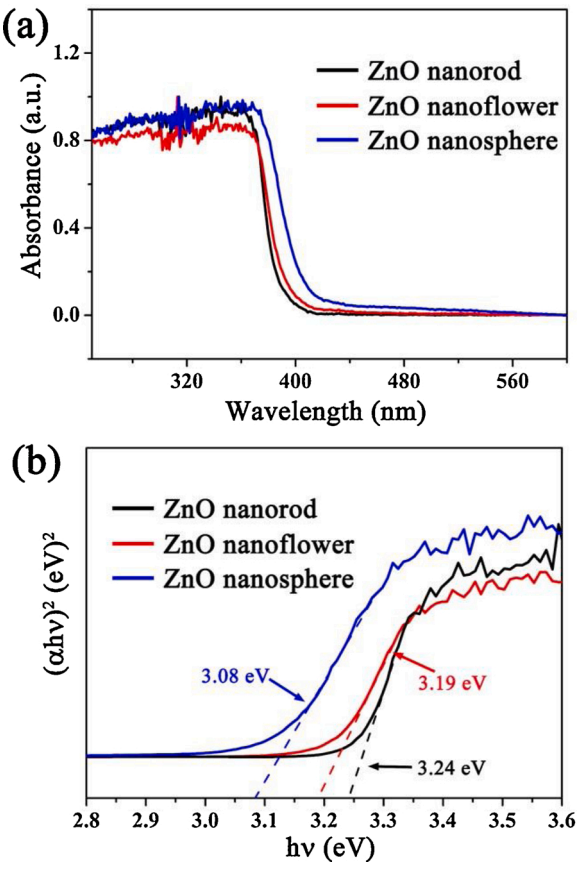

Fig. 4. (a) UV-visible absorption spectra and (b) the corresponding bandgap of three different ZnO nanostructures.

and surface chemisorbed oxygen species, respectively [27]. The peak position of ZnO nanoflowers have a little offset about 0.2 eV but can be negligible compared with other samples. For better comparison, the percentage of different components in O 1s of three different ZnO nanostructures were listed in Table 1. It can be known that ZnO nanorods have the lowest proportion of surface chemisorbed oxygen while ZnO nanospheres have the most, which is thought to play a very important role in the gas sensitivity process.

The N_2 adsorption-desorption isotherms of three different ZnO nanostructures were shown in Fig. 6. All of the ZnO showed the typical type IV adsorption-isotherms with a H_3-type hysteresis loop, indicating the presence of the mesoporous structure [28]. It can be seen that the specific surface area of ZnO nanospheres are much bigger than ZnO nanorods and ZnO nanoflowers. Generally speaking, high specific surface area can provide more adsorption active sites for the adsorption of oxygen molecules, which is in accordance with the results of XPS.

Electrochemical impedance spectra were conducted to explore the conductivity and the charge transfer kinetics of three different ZnO nanostructures. Fig. 7a displayed the Nyquist plots of ZnO nanorods, nanoflowers, and nanospheres. The inset is the Randle equivalent circuit, where R_s represents the electrolyte solution resistance, R_{ct} is the charge transfer resistance, Z_d is the Warburg impedance, and C_{dl} is the double layer capacitance [29]. It can be seen that the charge transfer resistance of ZnO nanorods are the minimum, indicating that its charge transfer is the fastest. Fig. 7b showed the corresponding Bode plots. The characteristic frequency peak of the ZnO nanorods shift to a higher frequency compared to that of the ZnO nanoflowers and ZnO nanospheres, indicating a foreshortened photoexcited carrier lifetime of the ZnO nanorods [30].

From the above characterization results, it can be seen that ZnO nanorods have lower defect density and faster charge transfer ability, while ZnO nanoflowers and ZnO nanospheres possess larger specific surface area and more surface adsorbed oxygen species.

3.2. NO_2 sensing performance

All gas sensitivity tests were performed at room temperature (25 °C). It is generally accepted that UV light can reduce the initial resistance of ZnO to realize the detection of NO_2 at room temperature. Furthermore, the photogenerated electron-hole pairs can largely improve the sensing response and the recovery speed [9,10]. In this work, the sensing performance of as-prepared ZnO in dark condition was not investigated because that their resistance without UV light illumination was beyond the measuring range of the used multimeter. The exposure time of all the sensor devices in NO_2 was 150 s, and the subsequent exposure interval in air was 250 s. Fig. 8a showed the transient response curves of ZnO nanorods, nanoflowers, and nanospheres in different NO_2 concentrations activated by UV light. It can be seen that all of the ZnO have complete response and recovery process, and the response increases with NO_2 concentration. For better comparison, the response curves as a function of NO_2 concentration were shown in Fig. 8b. It can be seen that ZnO nanospheres exhibit the highest response, and the response to NO_2 concentration of 0.1, 0.5, 1, 3, and 5 ppm is 1.4, 2.2, 3.8, 11.30, and 29.40, respectively. The response of ZnO nanoflowers is 1.3, 2.0, 3.3, 8.1, and 14.4, and the response of ZnO nanorods is 1.2, 1.6, 2.3, 4.5, and 4.5, respectively. When the concentration of NO_2 is low (less than 1 ppm), the surface of three different ZnO nanostructures has sufficient reactive sites for the gas-sensing reaction. Therefore, the sensing responses of three different ZnO nanostructures were not significantly different. However, once the concentration of NO_2 goes up, the active sites of ZnO nanorods tend to be saturated, but there are still enough active sites for additional gas-sensing reactions in ZnO nanoflowers and ZnO nanospheres. As a result, the responses of three different ZnO nanostructures are quite different at higher concentrations of NO_2. The same phenomenon can be seen in the published literatures [31,32]. Moreover, the saturation concentration of gas-sensing materials is related to the number of reactive sites on the surface. As the XPS results show, ZnO nanorods have the least surface chemisorbed oxygen. Therefore, ZnO nanorods would reach saturation at a low concentration of NO_2 while ZnO nanoflowers and ZnO nanospheres do not.

The response and recovery time of three different ZnO nanostructures in function of NO_2 concentration was shown in Fig. 8c and d, respectively. It can be seen that the response and recovery time of ZnO nanorods and nanoflowers decrease with the increase of NO_2 concentration while ZnO nanospheres do not show obvious regularity. The recovery time is longer than the response time is may be due to that the NO2 molecule has one unpaired electron, which facilitates its chemisorption on the surface of ZnO [33]. It is worth mentioning that the ZnO nanorods exhibit ultrafast response and recovery speed, which is faster than that of most of the reported literatures. The response time of ZnO nanorods is 23, 12, 10, 9, and 9 s, and the recovery time is 95, 35, 23, 18, and 18 s corresponding to 0.1, 0.5, 1, 3, and 5 ppm NO_2, respectively. It can be seen that ZnO nanospheres exhibit the highest response under UV irradiation. In contrast, ZnO nanorods show the fastest response and recovery speed. The ZnO nanoflowers are between ZnO nanorods and ZnO nanospheres no matter the sensing response or the response and recovery speed. The sensing response of ZnO nanoflowers increase 320 % compared with the ZnO nanorods while the ZnO nanospheres increase 650 %. The response time of ZnO nanorods shortened 310 % compared with the ZnO nanoflowers while shortened 1200 % compared with the ZnO nanospheres. The recovery time of ZnO nanorods shortened 220 % compared with the ZnO nanoflowers while shortened 1210 % compared with the ZnO nanospheres.

The reproducibility of three different ZnO nanostructures was also investigated. The transient response curves of ZnO nanorods, nanoflowers, nanospheres with time to 5 ppm NO_2 gas over four sequential cycles were presented in Fig.9a, respectively. In addition, for each

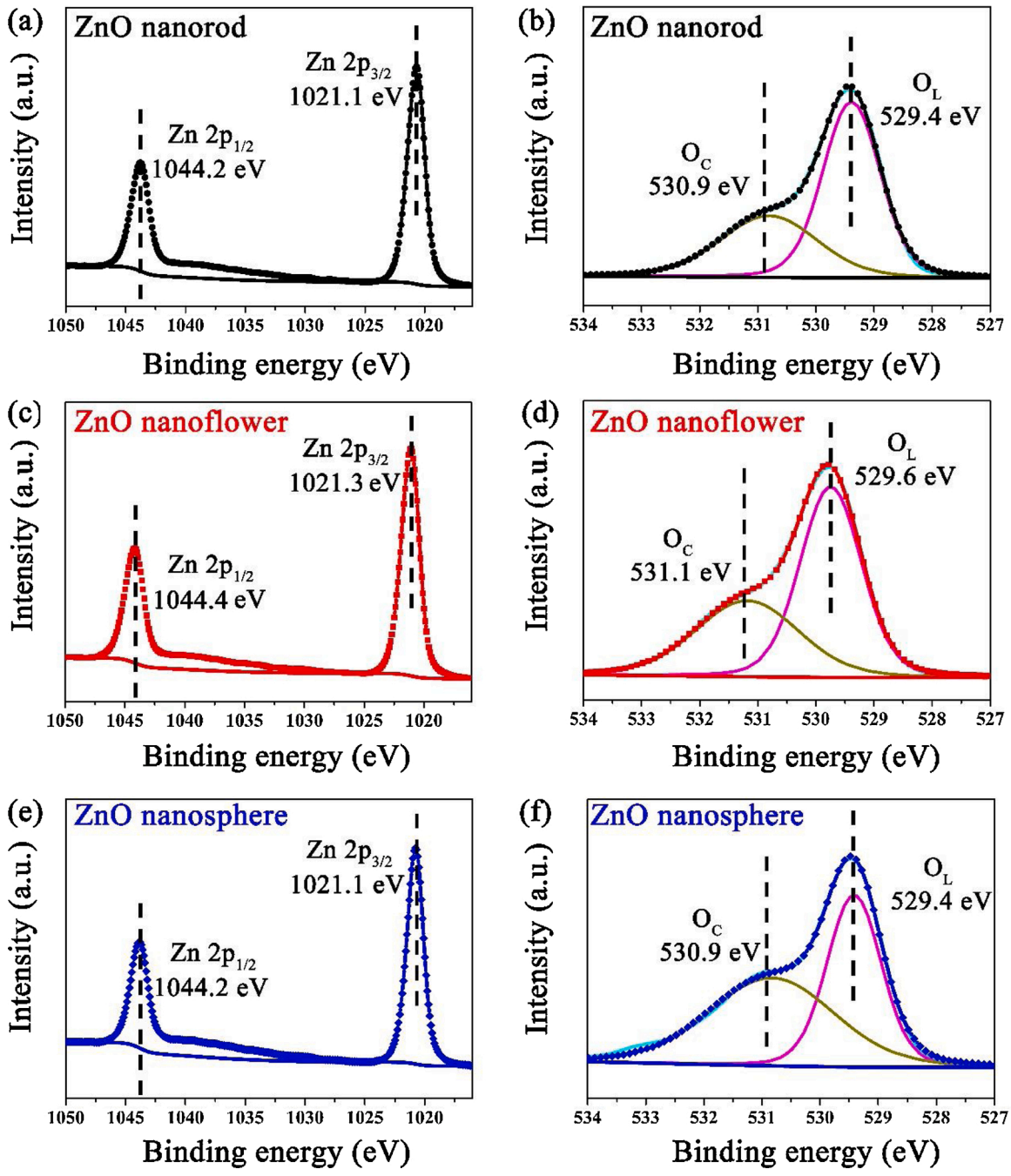

Fig. 5. The XPS spectra of (a) Zn 2p and (b) O 1s of ZnO nanorods; (c) Zn 2p and (d) O 1s of ZnO nanoflowers; (e) Zn 2p and (f) O 1s of ZnO nanospheres.

Table 1
The composition in O 1s of three different nanostructures of ZnO.

Samples	lattice oxygen (O_L)	chemisorbed oxygen (O_C)
ZnO nanorods	63.86 %	36.14 %
ZnO nanoflowers	58.78 %	41.22 %
ZnO nanospheres	45.55 %	54.45 %

sensing material, we fabricated three sensor devices for the reproducibility measurement and the results were shown in Fig. S2. The magnitude of response changes in each sensor device or each cycle is basically same, indicating their excellent reproducibility.

The response of three different ZnO nanostructures to some interfering harmful gases including NO, CO, NH_3, C_6H_6, H_2, ethanol, acetone (5 ppm to NO_2 and 100 ppm to other gases) was also investigated under UV light illumination at room temperature. As shown in Fig. 9b, all of the ZnO exhibit much higher response to NO_2 than other harmful gases, indicating their excellent selectivity. It can be attributed to the following factors. Firstly, the NO2 molecule has one unpaired electron, which facilitates its chemisorption on the surface of ZnO [33]. Secondly, NO2 molecule possesses the smallest bond energy about 312.7 kJ/mol. The bond energy of NO, CO, NH_3, and H_2 is 632.0, 1076.5, 1173.0, and 436.0 kJ/mol [34]. For the macromolecular gases such as C_6H_6, ethanol, acetone, their bond energy is going to be larger. A smaller bond energy is more conducive to the occurrence of sensing reaction, especially for sensors operated at room temperature. Therefore, three different ZnO nanostructures showed excellent selectivity to NO_2.

The effect of humidity on the sensing performance was also investigated. For gas sensors especially those operated at room temperature,

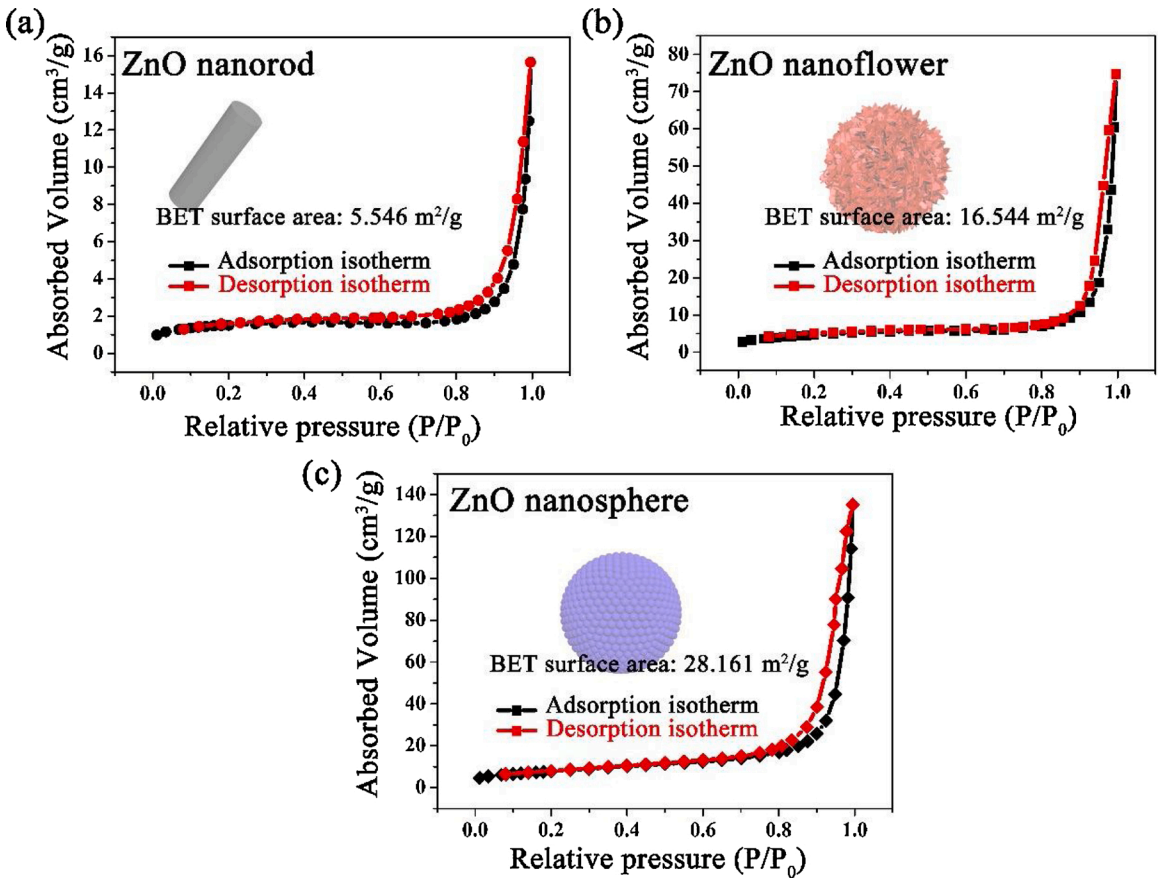

Fig. 6. N_2 gas adsorption-desorption isotherm for BET surface area analysis of three different ZnO nanostructures.

humidity level has a great effect on the gas-sensing response. UV light has been proved to be an effective approach to reduce the influence of physically adsorbed water and realize the minimum of cross-sensitivity of relative humidity [35]. However, the intensity of UV-LED in our work is very small (5 mW/cm^2). As a result, the elimination of UV light on the adsorbed water is not very obvious. The transient response curves of three different ZnO nanostructures to 3 ppm NO_2 in different humidity atmosphere were shown in Fig. 10a. To get a more intuitive view of the effect of humidity variations on the response, the response curves as a function of relative humidity were shown in Fig. 10b. Moreover, the initial resistance variation of three different ZnO nanostructures with the relative humidity increases was shown in Fig. S3. It can be seen that the initial resistance of three different ZnO nanostructures only have a slight change as the humidity increases while the response decreased significantly. The decrease in response is due to that the adsorbed water molecules occupy the adsorption sites on the surface and reduce the adsorption of oxygen. However, a complete response and recovery process of three different ZnO nanostructures was preserved, and the response is still acceptable.

A comparison with the previously reported literatures on the sensing performance of NO_2 gas sensors activated by UV light was shown in Table 2 [36], [37], [38], [39], [40], [41], [42]. It can be seen that as-prepared ZnO in this work show excellent NO_2 sensing performance compared with other reported literatures. Among them, ZnO nanospheres show higher response, whereas ZnO nanorods exhibit faster response and recovery speed. There are different types of NO_2 sensors such as catalytic combustion sensor, thermal conductivity cell sensor, electrochemical sensor, infrared gas sensor, ultrasonic gas sensor, and solid electrolyte gas sensor. At present, NO_2 sensors in the market is mainly electrochemical type, which need to work at high temperature and could not detect NO_2 gas at room temperature. The photoexcited NO_2 sensors proposed in this paper are devices operating at room temperature. Moreover, we have measured the solid electrolyte type oxygen sensor and catalytic combustion type methane sensor from the market using our gas-sensing measurement system and got relatively satisfactory sensing performance, which proved that our test system is trouble-free.

3.3. Sensing mechanism

The sensor elements were exposed to UV light throughout the entire response and recovery process. The role of UV light can be attributed to the following aspects. Firstly, UV light effectively increases the electron density in the conduction band and reduces the initial resistance of ZnO. Secondly, the photosorbed oxygen species ($O^-_{2(hv)}$) is more active than the chemisorbed oxygen species ($O^-_{2(gas)}$) [12], which increases the surface activity and makes the sensing reaction with NO_2 more likely to happen. Thirdly, the photogenerated holes can promote the desorption of NO_2 due to their strong oxidizing property. The detailed sensing process is as follows.

In air, oxygen molecules can adsorb on the surface of ZnO and capture electrons from the conduction band to form chemisorbed oxygen ion ($O^-_{2(gas)}$).

$$O_{2(gas)} + e^- \rightarrow O^-_{2(ads)} \quad (3)$$

When ZnO is under UV light illumination, electrons in the valence band can absorb the photon energy to jump into the conduction band and decrease the resistance of ZnO.

On one hand, the photogenerated holes promote the desorption of

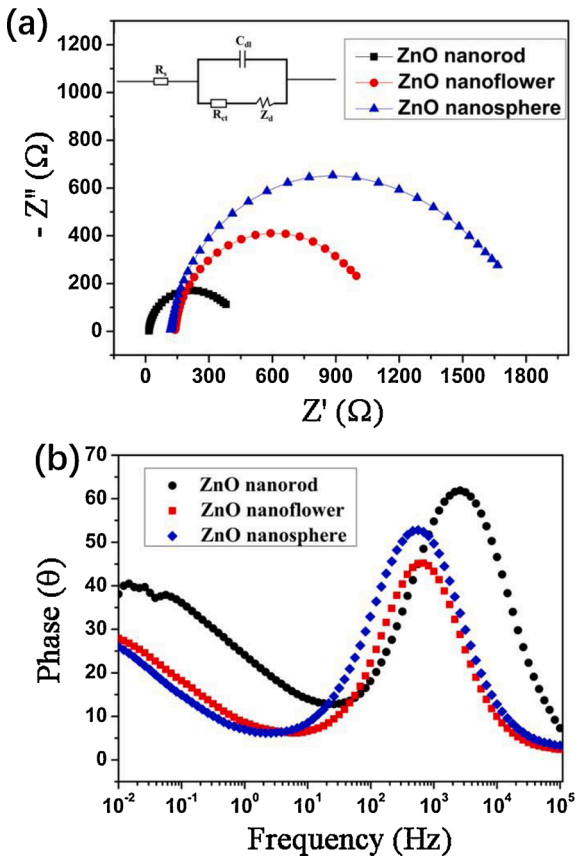

Fig. 7. The impedance spectroscopy of (a) Nyquist and (b) Bode plots of three different ZnO nanostructures. The inset is the Randle equivalent circuit.

chemisorbed oxygen ion ($O^-_{2(gas)}$. On the other hand, the oxygen molecules capture photogenerated electrons to generate the photosorbed oxygen species ($O^-_{2(hv)}$).

$$O^-_{2(gas)} + h^+_{hv} \rightarrow O_{2(gas)} \quad (4)$$

$$O_{2(gas)} + e^-_{h\upsilon} \rightarrow O^-_{2(h\upsilon)} \quad (5)$$

Once ZnO is exposed to NO_2 atmosphere, the electron density decreases due to that NO_2 molecules have a larger electronegative than oxygen molecules [43].

$$NO_2 + O^-_{2(hv)} \rightarrow NO^-_{2(hv)} + O_{2(gas)} \quad (6)$$

$$2NO_2 + O^-_{2(h\upsilon)} + e^-_{h\upsilon} \rightarrow 2NO^-_{3(hv)} \quad (7)$$

When ZnO is removed from NO_2 to air, the photogenerated holes can also promote the desorption of NO_2.

$$NO^-_{2(hv)} + h^+ \rightarrow NO_{2(gas)} \quad (8)$$

$$2NO^-_{3(hv)} + 2h^+ \rightarrow 2NO_{2(gas)} + O_2 \quad (9)$$

Three different ZnO nanostructures exhibited different sensing performance due to the differences in crystallinity, defect density, surface and electrical properties. The ZnO nanospheres show the highest response because of its biggest specific surface area and most adsorbed oxygen. The main resistance to electron transport in ZnO sensing layer is distributed at the grain boundary barrier. Firstly, ZnO nanorods have the best crystallinity, least defect density, which means that the depletion layer at the barrier is the thinnest and electrons are more easily transferred between crystal grains. Secondly, it can be seen that the average crystal size of ZnO nanorods calculated from Scherrer's formula is the biggest, which means that the amounts of grain boundary barrier in ZnO nanorods is the least. Thirdly, ZnO nanorods have the unidirectional

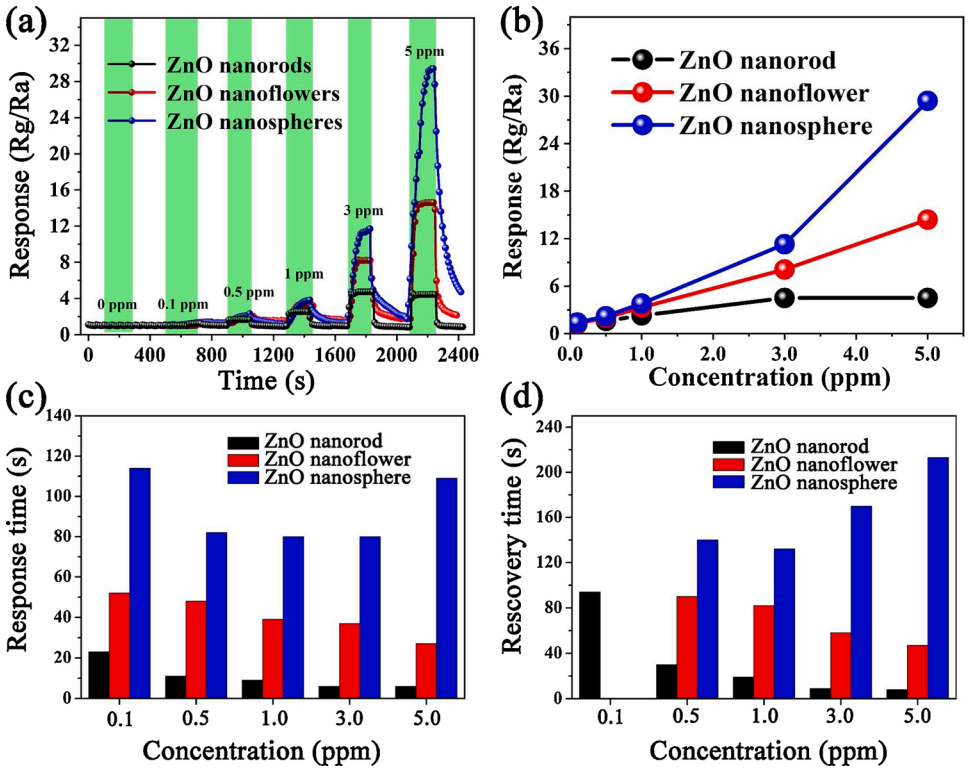

Fig. 8. (a) Dynamic response curves with time of three different ZnO nanostructures; (b) the response curves with NO_2 concentration of three different ZnO nanostructures; (c–d) the response and recovery time of three different ZnO nanostructures.

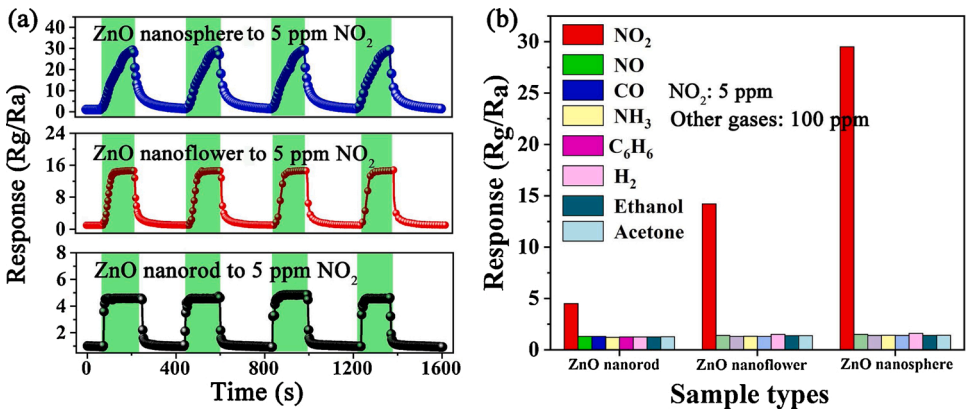

Fig. 9. (a) The repeatability of three different ZnO nanostructures to 5 ppm NO_2; (b) the selectivity of three different ZnO nanostructures to other harmful gases.

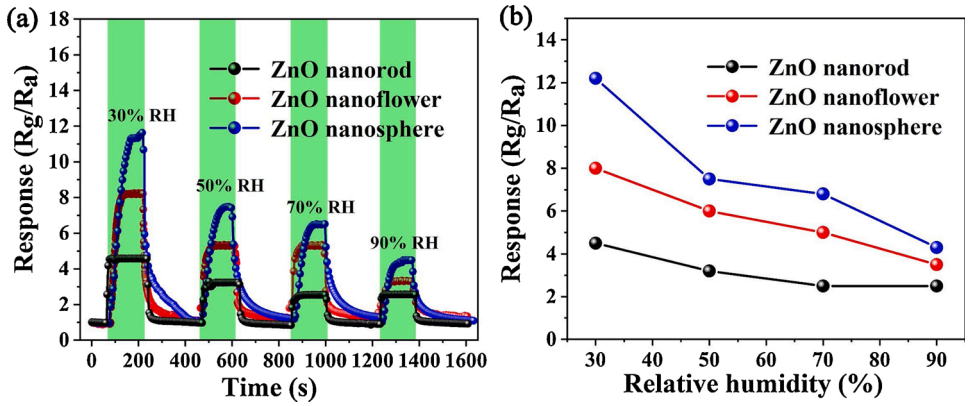

Fig. 10. (a) The dynamic response curves of three different ZnO nanostructures to 3 ppm NO_2 in different humidity atmosphere ranging from 30 % RH to 90 % RH; (b) the response curves with relative humidity of three different ZnO nanostructures.

Table 2
The sensing performance of NO_2 sensors activated by UV light at room temperature.

Materials	NO_2(ppm)	Response	T_{res} and T_{rec}	Excitation source	Ref
walnut-like In_2O_3	50	219	89 and 80 s	365 nm LED (1.2 mW/cm^2)	[36]
In_2O_3–rGO	30	8.25	360 and 1440 s	365 nm LED (no given)	[37]
PSS/ZnO nanowires	2	7	300 and 440 s	265 nm LED (0.5 mW/cm^2)	[38]
Au/MoS_2 thin film	2.5	30	~300 and 1000 s	365 nm LED (no given)	[39]
RGO/GeO_2	10	4.59	230 and 258 s	365 nm LED (0.25 mW/cm^2)	[40]
ZnO/In_2O_3 nanosphere	5	2.21	78 and 610 s	365 nm LED (25 mW/cm^2)	[41]
Pd/SnO_2 thick film	5	8	5 and >30 min.	365 nm LED (35 mW/cm^2)	[42]
ZnO nanorods	5	4.50	9 and 18 s	365 nm LED (5 mW/cm^2)	This work
ZnO nanoflowers	5	1.44	28 and 49 s	365 nm LED (5 mW/cm^2)	This work
ZnO nanospheres	5	2.94	116 and 215 s	365 nm LED (5 mW/cm^2)	This work

electron transfer path, which means that it has the shortest transmission path. Therefore, the speed of electron transmission in ZnO nanorods is the fastest, which has been proved by EIS measurements. As a result, the ZnO nanorods exhibit the fastest response and recovery speed.

4. Conclusion

In this work, three different ZnO nanostructures (nanorods/flowers/spheres) were successfully prepared by a facile hydrothermal method or water bath, whose surface and electronic characteristics were investigated through XRD, SEM, TEM, UV–vis, XPS, BET, EIS measurements. The sensing performance showed that ZnO nanospheres exhibit the highest response 29.4–5 ppm NO_2 activated by UV light at room temperature, which can be attributed to the most adsorbed oxygen species on the surface. ZnO nanorods show the fastest response and recovery speed (9 and 18 s to 5 ppm NO_2) due to the best crystallinity, least grain boundary, and the unidirectional electron transfer path. For NO_2 sensors operated at room temperature, no matter fast response and recovery speed or high sensing response is meaningful for practical application. Therefore, the combination of the ZnO nanorods and the ZnO nanospheres may realize a NO_2 sensor operated at room temperature with high sensitivity and fast response and recovery speed.

CRediT authorship contribution statement

Hongtao Wang: Conceptualization, Methodology, Formal analysis, Writing - original draft. **Meng Dai:** Software, Investigation. **Yueyue Li:** Resources, Data curation. **Jihao Bai:** Validation. **Yueying Liu:** Validation. **Yuan Li:** Validation. **Chenchang Wang:** Validation. **Fengmin Liu:** Writing - review & editing. **Geyu Lu:** Writing - review & editing.

Declaration of Competing Interest

The authors report no declarations of interest.

Acknowledgements

This work was supported by National Nature Science Foundation of China (Nos. 61871198, 61474057 and 61520106003), National key Research and Development Program of China (No. 2016YFC0201002).

Appendix A. Supplementary data

Supplementary material related to this article can be found, in the online version, at doi:https://doi.org/10.1016/j.snb.2020.129145.

References

[1] D. Zhang, Z. Liu, C. Li, T. Tang, X. Liu, S. Han, B. Lei, C. Zhou, Detection of NO_2 down to ppb Levels using individual and multiple In_2O_3 nanowire devices, Nano Lett. 10 (2004) 1919–1924.
[2] R. Kumar, O. Al-Dossary, G. Kumar, A. Umar, Zinc oxide nanostructures for NO_2 gas-sensor applications: a review, Nano-Micro Lett. 7 (2015) 97–120.
[3] C. Chang, C. Lin, J. Chen, M. Hsu, Ce-doped ZnO nanorods based low operation temperature NO_2 gas sensors, Ceram. Int. 40 (2014) 10867–10875.
[4] C. Baratto, G. Sberveglieri, A. Onischuk, B. Caruso, S. di Stasio, Low temperature selective NO_2 sensors by nanostructured fibres of ZnO, Sens. Actuators B 100 (2004) 261–265.
[5] A. Sharma, M. Tomar, V. Gupta, WO_3 nanoclusters-SnO_2 film gas sensor heterostructure with enhanced response for NO_2, Sens. Actuators B 176 (2013) 675–684.
[6] A. Chowdhuri, V. Gupta, K. Sreenivas, Fast response H_2S gas sensing characteristics with ultra-thin CuO islands on sputtered SnO_2, Sens. Actuators B 93 (2003) 572–579.
[7] S. Morandi, A. Fioravanti, G. Cerrato, S. Lettieri, M. Sacerdoti, M. Carotta, Facile synthesis of ZnO nano-structures: morphology influence on electronic properties, Sens. Actuators B 249 (2017) 581–589.
[8] Y. Li, M. Jiao, H. Zhao, M. Yang, High performance gas sensors based on in-situ fabricated ZnO/polyaniline nanocomposite: the effect of morphology on the sensing properties, Sens. Actuators B 264 (2018) 285–295.
[9] Q. Drmosh, A. Hendi, M. Hossain, Z. Yamani, R. Moqbel, A. Hezam, M. Gondal, UV-activated gold decorated rGO/ZnO heterostructured nanocomposite sensor for efficient room temperature H_2 detection, Sens. Actuators B 290 (2019) 666–675.
[10] Y. Chen, X. Li, X. Li, J. Wang, Z. Tang, UV activated hollow ZnO microspheres for selective ethanol sensors at low temperatures, Sens. Actuators B 232 (2016) 158–164.
[11] D. Haridas, A. Chowdhuri, K. Sreenivas, V. Gupta, Enhanced room temperature response of SnO_2 thin film sensor loaded with Pt catalyst clusters under UV radiation for LPG, Sens. Actuators B 153 (2011) 152–157.
[12] C. Zhang, A. Boudiba, P. Marco, R. Snyders, M. Olivier, M. Debliquy, Room temperature responses of visible-light illuminated WO_3 sensors to NO_2 in sub-ppm range, Sens. Actuators B 181 (2013) 395–401.
[13] G. Matzeu, L. Florea, D. Diamond, Advances in wearable chemical sensor design for monitoring biological fluids, Sens. Actuators B 211 (2015) 403–418.
[14] H. Choi, S. Kwon, W. Lee, K. Im, T. Kim, B. Noh, S. Park, S. Oh, K. Kim, Ultraviolet photoactivated room temperature NO_2 gas sensor of ZnO hemitubes and nanotubes covered with TiO_2 nanoparticles, Nanomaterials 10 (2020) 462.
[15] L. Qi, L. Yu, Z. Liu, F. Guo, Y. Gu, X. Fan, An enhanced optoelectronic NO2 gas sensors based on direct growth ZnO nanowalls in situ on porous rGO, Jalloy. Compd. 749 (2018) 244–249.
[16] L. Meng, Q. Xu, Z. Sun, G. Li, S. Bai, Z. Wang, Y. Qin, Enhancing the performance of room temperature ZnO microwire gas sensor through a combined technology of surface etching and UV illumination, Mater. Lett. 212 (2018) 296–298.
[17] Y. Zhang, Y. Liu, L. Zhou, D. Liu, F. Liu, F. Liu, X. Liang, X. Yan, Y. Gao, G. Lu, The role of Ce doping in enhancing sensing performance of ZnO-based gas sensor by adjusting the proportion of oxygen species, Sens. Actuators B 273 (2018) 991–998.
[18] Y. Zhang, D. Li, L. Qin, P. Zhao, F. Liu, X. Chuai, P. Sun, X. Liang, Y. Gao, Y. Sun, G. Lu, Preparation and gas sensing properties of hierarchical leaf-like SnO_2 materials, Sens. Actuators B 255 (2018) 2944–2951.
[19] Z. Zhang, C. Shao, X. Li, C. Wang, M. Zhang, Y. Liu, Electrospun nanofibers of p-Type NiO/n-type ZnO heterojunctions with enhanced photocatalytic activity, ACS Appl. Mater. Inter. 2 (2010) 2915–2923.
[20] P. Rai, Y. Yu, Synthesis of floral assembly with single crystalline ZnO nanorods and its CO sensing property, Sens. Actuators B 161 (2012) 748–754.
[21] J. Ghosh, R. Ghosh, P. Giri, Tuning the visible photoluminescence in Al doped ZnO thin film and its application in label-free glucose detection, Sens. Actuators B 254 (2018) 681–689.
[22] F. Li, F. Gong, Y. Xiao, A. Zhang, J. Zhao, S. Fang, D. Jia, ZnO twin-spheres exposed in ± (001) facets: stepwise self-assembly growth and anisotropic blue emission, ACS Nano 7 (2013) 10482–10491.
[23] J. Xu, Z. Xue, N. Qin, Z. Cheng, Q. Xiang, The crystal facet-dependent gas sensing properties of ZnO nanosheets: experimental and computational study, Sens. Actuators B 242 (2017) 148–157.
[24] J. Jiang, Z. Mu, H. Xing, Q. Wu, X. Yue, Y. Lin, Insights into the synergetic effect for enhanced UV/visible-light activated photodegradation activity via Cu-ZnO photocatalyst, Appl. Surf. Sci. 478 (2019) 1037–1045.
[25] M. Al-Hashem, S. Akbar, P. Morris, Role of oxygen vacancies in nanostructured metal-oxide gas sensors: a review, Sens. Actuators B 301 (2019), 126845.
[26] Y. Li, H. Yu, Y. Yang, X. Dong, Fabrication of 3D ordered mesoporous ball-flower structures ZnO material with the excellent gas sensitive property, Sens. Actuators B 300 (2019), 127050.
[27] P. Cao, Z. Yang, S. Navale, S. Han, X. Liu, W. Liu, Y. Lu, F. Stadler, D. Zhu, Ethanol sensing behavior of Pd-nanoparticles decorated ZnO-nanorod based chemiresistive gas sensors, Sens. Actuators B 298 (2019), 126850.
[28] P. Qiao, L. Zhang, M. Zhu, Y. Yin, Z. Zhao, H. Sun, J. Dong, L. Bie, Acetylene sensing enhancement of mesoporous ZnO nanosheets with morphology and defect induced structural sensitization, Sens. Actuators B 250 (2017) 189–197.
[29] Q. Bu, S. Li, K. Zhang, Y. Lin, D. Wang, X. Zou, T. Xie, Hole transfer channel of ferrihydrite designed between Ti-Fe_2O_3 and CoPi as an efficient and durable photoanode, ACS Sustain. Chem. Eng. 7 (2019) 10971–10978.
[30] F. Li, J. Li, J. Zhang, L. Gao, X. Long, Y. Hu, S. Li, J. Jin, J. Ma, NiO nanoparticles anchored on phosphorus-doped α-Fe_2O_3 nanoarrays: an efficient hole extraction p–n heterojunction photoanode for water oxidation, ChemSusChem 11 (2018) 2156–2164.
[31] S. Wei, S. Wang, Y. Zhang, M. Zhou, Different morphologies of ZnO and their ethanol sensing property, Sens. Actuators B 192 (2014) 480–487.
[32] J. Cui, L. Shi, T. Xie, D. Wang, Y. Lin, UV-light illumination room temperature HCHO gas-sensing mechanism of ZnO with different nanostructures, Sens. Actuators B 227 (2016) 220–226.
[33] H. Kim, Y. Kwon, A. Mirzaei, S. Kang, M. Choi, J. Bang, S. Kim, Synthesis of zinc oxide semiconductors–graphene nanocomposites by microwave irradiation for application to gas sensors, Sens. Actuators B 249 (2017) 590–601.
[34] U. Iftekhar, Y. Usman, P. Duy-Thach, C. Gwiy-Sang, A novel flexible acetylene gas sensor based on PI/PTFE-supported Ag-loaded vertical ZnO nanorods array, Sens. Actuators B 222 (2016) 536–543.
[35] T. Hyodo, K. Urata, K. Kamada, T. Ueda, Y. Shimizu, Semiconductor-type SnO_2-based NO_2 sensors operated at room temperature under UV-light irradiation, Sens. Actuators B 253 (2017) 630–640.
[36] H. Ma, L. Yu, X. Yuan, Y. Li, C. Li, M. Yin, X. Fan, Room temperature photoelectric NO_2 gas sensor based on direct growth of walnut-like In_2O_3 nanostructures, J. Alloys Compd. 782 (2019) 1121–1126.
[37] F. Gu, R. Nie, D. Han, Z. Wang, In_2O_3–graphene nanocomposite based gas sensor for selective detection of NO_2 at room temperature, Sens. Actuators B 219 (2015) 94–99.
[38] J. Wang, M. Yu, X. Li, Y. Xi, UV-enhanced NO_2 gas sensing properties of polystyrene sulfonate functionalized ZnO nanowires at room temperature, Inorg. Chem. Front. 6 (2019) 176–183.
[39] Y. Zhou, C. Zou, X. Lin, Y. Guo, UV light activated NO_2 gas sensing based on Au nanoparticles decorated few-layer MoS_2 thin film at room temperature, Appl. Phys. Lett. 113 (2018), 082103.
[40] J. Hu, C. Zou, Y. Su, M. Li, X. Ye, B. Cai, E. Kong, Z. Yang, Y. Zhang, Light-assisted recovery for a highly-sensitive NO_2 sensor based on RGO-CeO_2 hybrids, Sens. Actuators B 270 (2018) 119–129.
[41] E. Espid, F. Taghipour, Development of highly sensitive ZnO/In_2O_3 composite gas sensor activated by UV-LED, Sens. Actuators B 241 (2017) 828–839.
[42] F. Saboor, T. Ueda, K. Kamada, T. Hyodo, Y. Mortazavi, A. Khodadadi, Y. Shimizu, Enhanced NO_2 gas sensing performance of bare and Pd-loaded SnO_2 thick film sensors under UV-light irradiation at room temperature, Sens. Actuators B 223 (2016) 429–439.
[43] Z. Wang, G. Men, R. Zhang, F. Gu, D. Han, Pd loading induced excellent NO_2 gas sensing of 3DOM In_2O_3 at room temperature, Sens. Actuators B 263 (2018) 218–228.

Hongtao Wang is currently studying for Doctor's degree at Jilin University. His work is studying photoelectric gas-sensing based on metal oxide nanomaterials.

Meng Dai received the BS degree in Department of Micro-Electronics in 2018. She is currently studying for her M.E Sci degree in College of Electronic Science and Engineering, Jilin University, China.

Yueyue Li received the BS degree in Department of Micro-Electronics in 2019. She is currently studying for her M.E Sci degree in College of Electronic Science and Engineering, Jilin University, China.

Jihao Bai received the BS degree in Department of Electronic Science and Technology in 2018. He is currently studying for his M.E Sci degree in College of Electronic Science and Engineering, Jilin University, China.

Yueying Liu received the BS degree in Department of Electronic Science and Technology in 2017. She is currently studying for her M.E Sci degree in College of Electronic Science and Engineering, Jilin University, China.

Yuan Li received the BS degree in Department of Electronic Science and Technology in 2019. He is currently studying for his M.E Sci degree in College of Electronic Science and Engineering, Jilin University, China.

Chenchang Wang received the BS degree in Department of Micro-Electronics in 2019. She is currently studying for her M.E Sci degree in College of Electronic Science and Engineering, Jilin University, China.

Fengmin Liu received the BE degree in Department of Electronic Science and Technology in 2000. She received her Doctor's degree in College of Electronic Science and Engineering at Jilin University in 2005. Now she is a professor in Jilin University, China. Her current research is preparation and application of semiconductor oxide, especial in gas sensor and solar cell.

Geyu Lu received the B.Sci. degree in Electronic Sciences in 1985 and the M.Sci. degree in 1988 from Jilin University in China and the Dr.Eng. degree in 1998 from Kyushu University in Japan. Now he is a professor of Jilin University, China. His current research interests include the development of chemical sensors and the application of the function materials.